APS physics

CHORUS

This is the accepted manuscript made available via CHORUS. The article has been published as:

# Experimental test of strong pinning and creep in current-voltage characteristics of type-II superconductors

M. Buchacek, Z. L. Xiao, S. Dutta, E. Y. Andrei, P. Raychaudhuri, V. B. Geshkenbein, and G. Blatter

Phys. Rev. B **100**, 224502 — Published 4 December 2019

DOI: 10.1103/PhysRevB.100.224502

# Experimental test of strong pinning and creep in current–voltage characteristics of type II superconductors

M. Buchacek,[1] Z. L. Xiao,[2] S. Dutta,[3] E. Y. Andrei,[4] P. Raychaudhuri,[3] V.B. Geshkenbein,[1] and G. Blatter[1]

[1] *Institute for Theoretical Physics, ETH Zurich, 8093 Zurich, Switzerland*
[2] *Materials Science Division, Argonne National Laboratory, Lemont, IL 60439, USA*
[3] *Tata Institute of Fundamental Research, Homi Bhabha Road, Colaba, Mumbai 400005, India*
[4] *Department of Physics and Astronomy, Rutgers University, Piscataway, New Jersey 08855, USA*

(Dated: November 11, 2019)

Pinning and creep determine the current–voltage characteristic of a type II superconductor and thereby its potential for technological applications. The recent development of strong pinning theory provides us with a tool to assess a superconductor's electric properties in a quantitative way. Motivated by the observation of typical excess-current characteristics and field-scaling of critical currents, here, we analyze current–voltage characteristics measured on 2H-$NbSe_2$ and $a$-MoGe type II superconductors within the setting provided by strong pinning theory. The experimentally observed shift and rounding of the voltage-onset is consistent with the predictions of strong pinning in the presence of thermal fluctuations. We find the underlying parameters determining pinning and creep and discuss their consistency.

## I. INTRODUCTION

Topological excitations appearing in the ordered phase of many materials have a strong impact on their physical properties. Such excitations interact with material's defects, what modifies both the structural and dynamical properties of the topological superstructure and of the host material itself. In type-II superconductors, the topological objects appear in the form of vortices due to (current-)induced or applied magnetic fields [1]. While free moving vortices result in a finite resistivity [3], pinning the vortices to material defects [4] helps maintaining the superconductor's dissipation-free transport of electric current. In the absence of fluctuations, vortex motion only appears upon exceeding the critical current $I_c$. Thermal fluctuations potentially modify this picture by allowing for a slow, creep-type vortex motion even at subcritical drives $I < I_c$ that leads to a shift and smoothing of the transition in the critical region. In this paper, we make use of the quantitative results from strong pinning theory [5 and 6] in order to unambiguously identify vortex-creep in the critical region of the current–voltage characteristic of two distinct low-$T_c$ materials, 2H-$NbSe_2$, with $T_c = 7.18\,\mathrm{K}$ [7], see Fig. 1, and $a$-MoGe, with $T_c = 6.9\,\mathrm{K}$ [8], see Fig. 2.

The origins of pinning and creep can be traced back to the seminal papers of Anderson, Kim, and collaborators [4, 9, and 10], where Abrikosov vortices pinned onto defects were taken responsible for the properties of current transport in hard superconductors. Besides setting a focus on the Bean critical state [11] and its log-time decay, the shape of the current–voltage characteristic in the critical region was discussed as well, including an interpolation formula describing the transformation of creep-type to flow-type response of vortices that prevail at low and high drives, respectively [9]. Later, much further work has been devoted to studying creep, particularly in the high-$T_c$ superconductors where thermal fluctuations play an important role. On the one hand, relaxation experiments at low drives helped to identify glassy physics characterized by diverging barriers [12], while resistive measurements using sensitive voltmeters served the similar purpose of identifying a non-linear, i.e., glassy response [13]. However, less attention was given to the behavior in the critical region, e.g., the vanishing of barriers near $j_c$ or the smoothing of the characteristic. Not least, this is due to the inadequacy of pinning theories to make quantitative predictions, a deficiency that was overcome only recently, at least for the case of strong pinning [5 and 6].

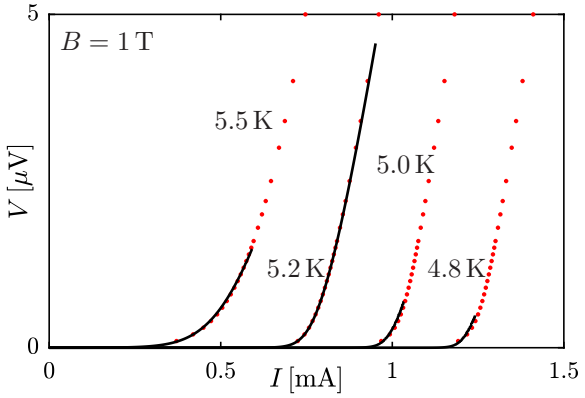


FIG. 1. Current–voltage characteristic measured on a 2H-$NbSe_2$ sample at a fixed field $H = 1.0\,\mathrm{T}$ and temperatures $T = 4.8$, 5.0, 5.2, and 5.5 K (red points). Black lines are fits to the data based on the prediction of strong pinning theory; fits are restricted to the region of applicability of the theory (see text for details). With increasing temperatures, the characteristic shifts to the left and the rounding in the critical region at voltage onset becomes more pronounced.

A distinctive feature of strong pinning is its excess-

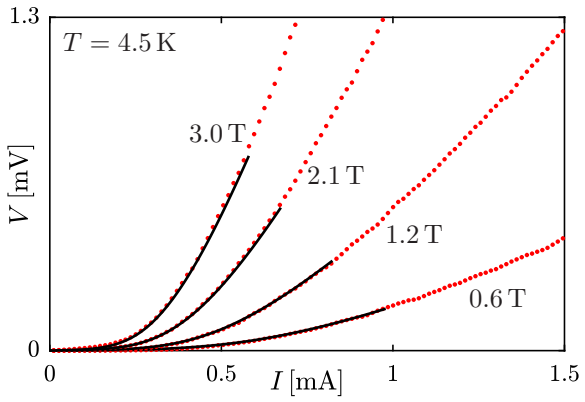


FIG. 2. Current–voltage characteristic measured on a $a$-MoGe sample at fixed temperature $T = 4.5\,\mathrm{K}$ and applied fields $H = 0.6, 1.2, 2.1$ and $3.0\,\mathrm{T}$ (red points). Black lines are fits to the data based on the prediction of strong pinning theory; fits are restricted to the region of applicability of the theory (see text for details). With increasing fields, the characteristic shifts to the left and the slope of the flux-flow response at large currents increases.

current characteristic, an $I - V$ characteristic that exhibits a linear (flux-flow) response at large drives $I > I_c$ that is shifted by the critical current $I_c$ [14 and 15], in an idealized $T = 0$ situation $V = R_{\mathrm{ff}}(I - I_c)\Theta(I - I_c)$ with $R_{\mathrm{ff}}$ the flux-flow resistance. Apart from the experiments [7 and 8] analyzed here, such characteristics have been observed in other recent [16] as well as older, even textbook [17] experiments. The analysis and proper understanding of changes in this $I$–$V$ characteristic with increasing temperature $T$ is the central topic of this work and involves the following goals: i) demonstrate the power and consistency of strong pinning theory in quantitatively explaining experimental data of $I$–$V$ characteristics in different materials for different temperatures $T$ and magnetic fields $B$. ii) Extract fitting parameters and check for their qualitative consistency with expectations from vortex theory as obtained within the Ginzburg-Landau (GL) phenomenological framework.

In pursuing this program, we have to disentangle two effects of temperature $T$, one being encoded in the parameter $\tau = 1 - t = 1 - T/T_c$ that appears in the Ginzburg-Landau (GL) mean-field theory of the superconducting state, the other being the temperature $T$ as the driver of thermal fluctuations. While the former lives on the scale $T_c$, the scale of the latter is given by the fluctuation energy $\xi\varepsilon_0$, with $\varepsilon_0 = (\Phi_0/4\pi\lambda)^2$ the vortex line energy, $\Phi_0 = hc/2e$ is the magnetic flux quantum, and $\xi$, $\lambda$ denote the correlation- and screening lengths of the superconductor. A further dependence is due to the presence of the magnetic field (or more precisely, induction) $B$, introducing the distance $\tau_b = 1 - T/T_c - B/H_{c2}(0) = 1 - t - b$ from the upper critical field-line $H_{c2}(T)$.

The critical current $I_c$ and the flux-flow resistance $R_{\mathrm{ff}}$, the parameters quantifying the shape of the excess-current characteristic, depend on the temperature $T$ and magnetic field $B$ via $\tau$ and $b$ (or $\tau_b$); approaching the $H_{c2}(T)$-line in the $H$–$T$ phase diagram, $I_c(B,T)$ decreases, see Fig. 1, and the flux-flow becomes steeper, see Fig. 2, with $R_{\mathrm{ff}}$ approaching the normal-state resistance $R_n$. Although these GL predictions are in rough agreement with experimental data, they do not catch effects of thermal fluctuations that are manifest in the data as well. In particular, within strong pinning theory, the inclusion of fluctuations predicts a further downward shift in the excess current, replacing the critical current $I_c$ by the depinning current $I_{\mathrm{dp}}(T)$, and a rounding of the transition to the ohmic branch of the characteristic [5 and 6].

A consistent analysis of creep phenomena then requires to separate these different types of temperature dependence in the experimental data. In our analysis, we achieve this task by rescaling the data to make it collapse onto one curve at asymptotically large drives. The comparison of the temperature-dependent rounding and shift of the collapsed data in the critical region around $I_{\mathrm{dp}}$ with the prediction from strong pinning theory then provides clear evidence for vortex creep, see Figs. 3 and 5. In figures 1 and 2, we show the corresponding fits to the original experimental data that demonstrate an impressive agreement. Furthermore, our quantitative theory allows to extract important parameters of vortex physics from the data and check for their internal consistency. Note the difference to the celebrated theory of weak collective pinning [18 and 19], where the addition of forces due competing defects poses a formidable task; the latter is straightforward within the strong pinning paradigm where the density $n_p$ of defects is assumed to be small such that pins act individually. As a consequence, results obtained within strong pinning theory can be pushed to provide a numerical accuracy beyond what can be achieved within the framework of weak collective pinning. In particular, strong pinning theory, here in its simplest version assuming point-like defects, can offer quantitative expressions for critical current densities [20], current–voltage characteristics [14 and 15], and thermal creep in the critical regime [5 and 6].

In the following, we first introduce and discuss the result for the current–voltage characteristic as obtained from strong pinning theory [5 and 6], see Sec. II. In Sec. III, we present the experimental data on the current–voltage characteristics of 2H-$NbSe_2$ and $a$-MoGe and extract the parameters of the characteristic. Sec. IV is devoted to the analysis of creep barriers, where we put forward a new type of analysis that aims at $U(F_{\mathrm{pin}})$, i.e., the barrier's dependence on the pinning-force density $F_{\mathrm{pin}}$ rather than the usual dependence $U(F_{\mathrm{L}})$ involving the Lorentz-force density $F_{\mathrm{L}}$ that drives the vortices. In Sec. V, we relate the parameters in the current–voltage characteristic as obtained from the comparison with experimental data to the 'microscopic' parameters of strong pinning theory; we summarize our results in Sec. VI and

provide some concluding remarks.

## II. CURRENT–VOLTAGE CHARACTERISTIC

We discuss the excess-current characteristic in the presence of thermal fluctuations (creep) as derived within the strong pinning paradigm. Within standard vortex physics, the relation between the driving current density $j$ and the vortex velocity $v$ is obtained from the dissipative equation of motion balancing the effects of the current-induced Lorentz force density $F_{\rm L}(j) = jB/c$ driving the vortices, the pinning force density $F_{\rm pin}(v,T)$ due to the defects, and the viscous force density $-\eta v$ proportional to the vortex velocity $v$,

$$\eta v = F_{\rm L}(j) - F_{\rm pin}(v,T). \qquad (1)$$

In the absence of thermal creep ($T = 0$) and at low velocities, strong pinning theory predicts a nearly constant pinning-force density $F_{\rm pin} \approx F_c$, $F_c$ the critical force density, over a large regime of velocities [14 and 15], in agreement with Coulomb's law of friction. For small currents, the driving Lorentz force then can be compensated by the pinning force and vortices remain pinned, $v = 0$. A finite vortex velocity $v \approx (F_{\rm L}(j) - F_c)/\eta > 0$ only appears at larger drives; as a result, we find the excess-current characteristic with vanishing voltage below the critical current density $j_c = cF_c/B$ and a shifted ohmic branch above. This seemingly trivial result owes its validity to the separation of the two velocity scales $v_c \ll v_p$ describing the average motion $v_c = F_c/\eta$ of the vortex lattice and the velocity $v_p \sim f_p/\eta a_0^3$ of vortices during individual (de-)pinning events (with $f_p$ the pinning force of an individual defect and $a_0 = \sqrt{\Phi_0/B}$ the separation between vortices); as shown in Refs. [14 and 15], the pinning-force density $F_{\rm pin}(v, T = 0)$ changes with velocity on the scale $v_p$.

At finite temperature $T > 0$, thermal creep facilitates the escape of vortices from pinning defects; such creep motion is characterized by an energy barrier $U(v)$ which relates to the velocity $v$ of vortices via

$$U(v) \approx k_{\rm B}T \log(v_{\rm th}/v). \qquad (2)$$

Here, $v_{\rm th}$ is the thermal velocity scale, related to an attempt frequency for thermal depinning and derived within strong pinning theory in Refs. [5 and 6], see also Sec. V. On approaching the thermal velocity scale $v_{\rm th}$, vortices traverse the pins sufficiently fast and the barrier slowing down the motion becomes irrelevant. The second central result provided by strong pinning theory is the force-dependence of these very same barriers, which assumes the simple form

$$U[F_{\rm pin}(v,T)] \approx U_c\,[1 - F_{\rm pin}(v,T)/F_c]^{3/2}. \qquad (3)$$

This result involves two noteworthy features: first, the relevant force in this simple relation is not the usual driving Lorentz-force density $F_{\rm L} \propto j$ (that would result in a standard relation [19] $U(j)$) but it is the pinning-force density $F_{\rm pin}(v,T)$. Second, the exponent $3/2$ is universal for any smooth pinning potential; its origin is found [6] in the thermally induced shift $\delta x$ of the (de-)pinning point which relates to the barrier $U$ via the scaling $U \propto \delta x^{3/2}$. A detailed derivation of $U_c$ is given in Refs. [5 and 6], see also Sec. V. The two equations (2) and (3) combine into a velocity and temperature dependence of the pinning force density $F_{\rm pin}(v,T)$ in the form

$$F_{\rm pin}(v,T)/F_c \approx 1 - [(k_{\rm B}T/U_c)\log(v/v_{\rm th})]^{2/3}. \qquad (4)$$

Inserting the expression for $F_{\rm pin}(v,T)$ into the equation of motion Eq. (1) and dividing by $F_c$, we arrive at a simple formula [5 and 6] for the fluctuation-enhanced vortex velocity or current–voltage characteristic,

$$v/v_c = j/j_c - 1 + \big[(k_{\rm B}T/U_c)\log(v_{\rm th}/v)\big]^{2/3}. \qquad (5)$$

Here, we have used the definition of the free flux-flow velocity $v_c = F_c/\eta$ at $F_c$. The dynamical equation (5) captures the small vortex velocity at subcritical drives $j < j_c$, the rounding of the characteristic in the critical region, and the (initial part) of the smooth approach to the ohmic region. As $v$ approaches $v_{\rm th}$, thermal fluctuations become irrelevant and the characteristic joins the excess-current shape.

The calculation leading to Eq. (5) is based on Kramers' rate theory [21 and 22] assuming an activation barrier $U_c \gg k_{\rm B}T$. Strong pinning theory tells [5], that the relevant barrier depends on velocity via $U \approx k_{\rm B}T\log(v_{\rm th}/v)$, see Eq. (2), that restricts the applicability of Eq. (5) to $v \lesssim v_{\rm th}/e$, see Figs. 1 and 2.

We relate the theoretical result (5) to the experimentally accessible current $I = Aj$ and voltage $V = LE$ ($E = Bv/c$ the electric field) using the sample geometry (length $L$ and area $A$) and the definition of the free flux-flow voltage at $I_c$, $V_c = R_{\rm ff}I_c$,

$$V = R_{\rm ff}(I - I_c) + V_c\Big[\frac{k_{\rm B}T}{U_c}\log\Big(\frac{v_{\rm th}}{v_c}\frac{V_c}{V}\Big)\Big]^{2/3}. \qquad (6)$$

This result can be directly compared to the data; it involves the four parameters $I_c, R_{\rm ff}, U_c/k_{\rm B}T, v_{\rm th}/v_c$ that are obtained in two steps. At large voltages $V$ (or velocities $v$), creep is irrelevant and the characteristic reduces to the simple exccess-current form $V \approx R_{\rm ff}(I - I_c)$, from which $I_c$ and $R_{\rm ff}$ can be directly read off. In a next step, we rescale the data $V \to V/V_c = v/v_c$ and $I \to I/I_c = j/j_c$ to bring it to the form of Eq. (5). This rescaling induces a data collapse in the asymptotic region; the deviations appearing in the transition region then are due to creep. It is this deviation from which we can extract the two remaining parameters $U_c/k_{\rm B}T$ and $v_{\rm th}/v_c$ through a careful fit to the experimental data in the transition region.

## III. EXPERIMENTAL CURRENT-VOLTAGE CHARACTERISTICS

We illustrate the procedure outlined above for fitting the data and extracting the relevant physical parameters $j_c, v_c, U_c, v_{\rm th}$ for the two low-$T_c$ superconductors 2H-$NbSe_2$ and $a$-MoGe.

### A. 2H-$NbSe_2$

The original experimental work reported in Ref. [7] describes a procedure for separating edge- and bulk contributions to the current–voltage characteristics of 2H-$NbSe_2$. This involves cutting the sample between subsequent measurements to adjust its width and comparing the characteristics before and after cutting. In our analysis below, we focus on such properly reduced bulk data taken at temperatures $T = 4.8$, 5.0, 5.2, and 5.5 K and exhibiting a pronounced excess-current characteristic; this bulk data has not been reported in the original publication [7]. The measurements were performed in a $H = 1$ T field directed along the $c$-axis with an in-plane dc current applied through the cross-sectional area $A = d\,w$, $d = 0.02$ mm, $w = 0.47$ mm (width after cutting) in a sample of length $L = 8$ mm. The inter-vortex distance $a_0 = \sqrt{\Phi_0/B} \approx 45$ nm is small compared to the sample thickness $d$ and hence the standard strong pinning theory for 3D bulk pinning [23] is applicable. Fig. 3 shows the data and fitting to Eq. (5) in the critical region, with the fits restricted to the region $v \lesssim v_{\rm th}/{\rm e}$ where our theory applies.

At high velocities $v > v_{\rm th}$, creep is irrelevant and we fit the data to the excess-current characteristic $V = R_{\rm ff}(I - I_c)$, see blue lines in Fig. 3(b). Analyzing the four curves at $T = 4.8$, 5.0, 5.2, and 5.5 K, we obtain the critical current densities $j_c = 13$, 11, 9.6, and 7.3 A/cm$^2$. These values are far below the $(T = 0)$ depairing current density $j_0 \approx 6.7 \times 10^7$ A/cm$^2$, consistent with a small defect density $n_p$, see Sec. V, and decrease on approaching the $H_{c2}$-line, $\tau_b = 1 - t - b \to 0$, see Fig. 4(a). From the slopes, we obtain the flux-flow resistivities $\rho_{\rm ff}$ and using the normal state resistivity $\rho_n \approx 6.9 \times 10^{-3}\,\Omega$cm, we verify the consistency with the Bardeen-Stephen result $\rho_{\rm ff}/\rho_n \approx B/H_{c2}$, see Fig. 4(b). The vortex motion generates the electric field $V/L = E = Bv/c$ and we obtain the estimates for the free flux-flow velocities $v_c = cV_c/BL = (0.52, 0.47, 0.45, 0.38)\,{\rm cm}\cdot{\rm s}^{-1}$.

While the original data include the intrinsic field- and temperature dependences of $j_c$ together with the rounding in the critical region, the rescaled data $V/V_c = v/v_c$ and $I/I_c = j/j_c$ in Fig. 3(c) collapse at high velocities to a single line of unit slope; the temperature-dependent rounding and shift of the curves away from the excess-current characteristic in the critical region then can be firmly attributed to thermal creep and serves to find the remaining parameters $U_c/k_{\rm B}T$ and $v_{\rm th}/v_c$.

Let us then focus on the most interesting part of the characteristic, the smooth transition to flux-flow in the critical region around $j_c$, see Fig. 3(a). In Sec. IV below, we present a protocol for the optimal extraction of these parameters by replotting the current-voltage data in a form that accounts for the creep-type motion in this regime. Inserting the results back into the characteristic (5), we obtain excellent fits to the data; the extracted barrier $U_c$ of order 1000 K rapidly decreases when approaching the $H_{c2}$-line, $\tau_b = 1-t-b \to 0$, see Fig. 4(c), in agreement with strong pinning theory and further discussion in Sec. V. Finally, the results for the thermal velocity parameter $v_{\rm th}/v_c$ are shown in Fig. 4(d). The discussion in Sec. V predicts an increase of $v_{\rm th}/v_c$ with temperature that is consistent with the experimental findings; the drop near the phase boundary may be due to a collapse of strong pinning $\kappa \to 1$. Its numerical value turns out about an order of magnitude larger than expected from strong pinning theory, however, we note that we have least control on this quantity since it assumes the role of an attempt frequency in Kramer's rate theory, a quantity that is notoriously difficult to calculate.

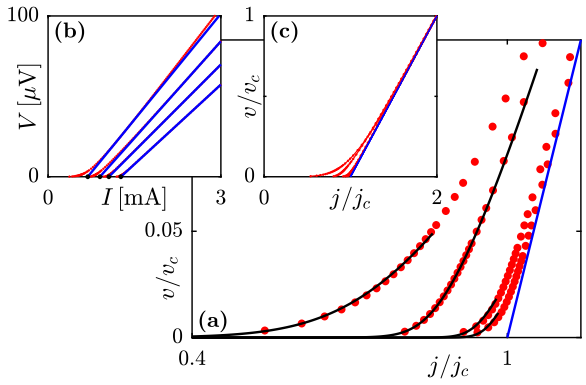


FIG. 3. Observation of thermal creep in 2H-$NbSe_2$. (a): evolution of excess-current characteristic with increasing temperature $T$: red data points are taken at $B = 1.0$ T, $T = 4.8$, 5.0, 5.2 and 5.5 K, black lines are fits to Eq. (5) describing the creep characteristic within strong pinning theory. Large temperatures produce a marked rounding of the characteristic in the critical region near voltage onset and the $T = 0$ excess-current characteristic (solid blue) is approached at larger drives. Fits are shown up to velocities where activation barriers remain larger than temperature $T$. Inset (b) shows the raw experimental data, see Fig. 1, while the inset (c) presents the data collapsed to a single curve at large drives; such scaling provides the parameters $j_c$ and $v_c$.

### B. $a$-MoGe

In a similar fashion, we analyse the $I$-$V$ measurements on $a$-MoGe films, with data available in the field range $H = 0.03 - 7$ T, up to order half the upper-critical field $H_{c2}(0) = 13$ T, and temperatures $T = 0.28$, 0.45, 2.0, 3.5, 4.5 and 5.5 K; some of this data has

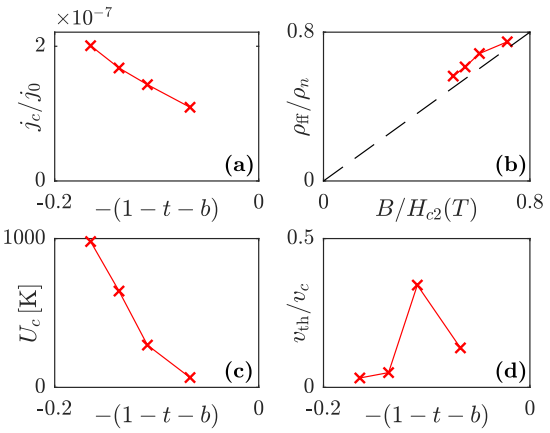


FIG. 4. Parameters for 2H-$NbSe_2$ extracted from fitting the $I$–$V$ characteristics of Fig. 3 as a function of $-\tau_b = -(1-t-b)$ chosen such as to approach the $H_{c2}$ line from the left (as in the standard $H$–$T$ diagram). The small value of the scaling parameter $j_c/j_0$ in (a) testifies for a small defect density $n_p$. The flux-flow resistivity shown in (b) follows the Bardeen-Stephen law $\rho_{ff}/\rho_n \approx B/H_{c2}(T)$ (dashed line). The activation barrier $U_c$ decays on approaching the upper-critical field line, see (c), while the scaled thermal velocity $v_{th}/v_c$ shown in (d) first rises on approaching the $H_{c2}$-line and then drops, that can be consistently explained by strong pinning theory, see Sec. V.

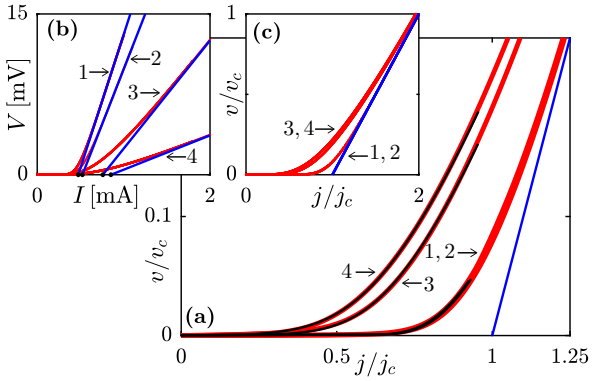


FIG. 5. (a) Extrapolated $T = 0$ excess-current characteristic (blue) and experimental data (red) at finite temperatures 1: 0.28 K, 1.2 T, 2: 0.45 K, 1.0 T (these two datasets collapse to an almost identical curve), 3: 2.0 K, 0.5 T, and 4: 3.5 K, 0.2 T. Thermal fluctuations produce a dowmward shift and rounding of the characteristic in the critical regime. Black lines provide excellent fits within strong pinning theory; the fit stops when barriers $U_c$ approach $k_BT$. The insets (b) and (c) show the raw and rescaled experimental data.

been reported before in Ref. [8]. The above magnetic fields produce vortex lattices with a lattice constant in the range $a_0 = 17 - 262$ nm. The thickness of the film measures $d = 20$ nm and its width is $w = 300\,\mu$m; while $d > a_0$ above $H \sim 4$ T, the low-field region may crossover to 2D pinning, see further discussion below. The current $I$ is applied along the direction of the film of length $L = 1$ mm.

The discussion in Ref. [8] has focused on the current-response at low drives $j \to 0$, where a linear resistivity has been taken as the signature of a vortex liquid phase. Here, we apply the strong pinning paradigm to explain the experimental data near the critical current $j_c$; interestingly, strong pinning theory also predicts a linear resistivity at low drives as barriers $U(j)$ saturate at small currents $j$, see Ref. [6]. In Fig. 5, we provide examples of $I - V$ curves taken at finite temperatures $T = 0.28$, 0.45, 2, and 3.5 K. The results of the scaling collapse of this data, providing the parameters $j_c$ and $\rho_{ff}$, are shown in Fig. 6. Making use of field-dependent data, we find that the critical current density scales as $j_c \sim B^{-\alpha}$ (Fig. 6(a), with $j_0 \approx 6.8 \times 10^6$ A/cm$^2$) with the exponent $\alpha \approx 0.6$ measured at low temperatures, consistent with theoretical predictions for the strong pinning scenario [15, 20, and 24]. The exponent decreases towards $\alpha \approx 0.3$ at higher temperatures, in agreement with numerical simulations [25] reporting such a behavior with increasing vortex core size. At low fields, a crossover to 2D or 1D strong pinning may occur, see discussion in Sec. V below. The resistivity extracted from the flux-flow regime above $j_c$ remains below the Bardeen-Stephen estimate (see Fig. 6(d), $\rho_n \approx 1.57 \times 10^{-4}\,\Omega$ cm), that is qualitatively consistent with a more elaborate result of Larkin and Ovchinikov [26]. The flux-flow vortex velocities corresponding to the analyzed data range between $v_c = 1 \times 10^3$ cm/s and $4 \times 10^3$ cm/s.

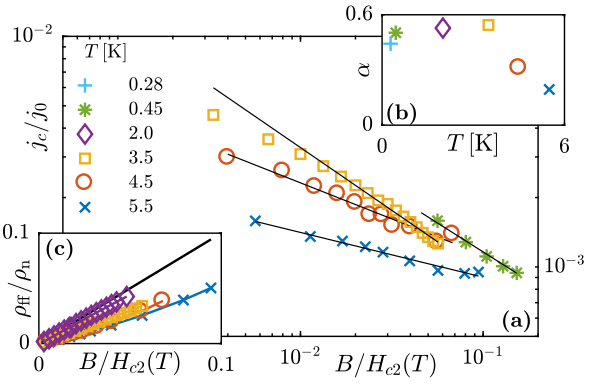


FIG. 6. (a) Critical current densities (a) versus magnetic field fitted to a power law $j_c \propto B^{-\alpha}$, with the exponents $\alpha$ at different temperatures shown in (b). The exponent $\alpha \approx 0.5$ is in good agreement with the prediction from strong pinning theory, and its decrease at high temperatures matches recent numerical results [25]. (c) Flux-flow resistivity compared to the Bardeen-Stephen formula (solid line); values below the Bardeen-Stephen line are consistent with more detailed predictions of Larkin and Ovchinikov [26].

In a second step, we focus on the transition region of the rescaled data of Fig. 5(a). While the curves at

higher temperatures are rounded and shifted away from the excess-current characteristic, the data taken at the two lowest temperatures collapse to an almost identical curve after rescaling; note that the reduced temperatures $\tau_b$ are nearly equal for the two curves, $\tau_b \approx 0.87$ versus $\tau_b \approx 0.86$ for the curves 1 and 2, while the temperature $T$, quantifying thermal fluctuations, increases by a factor $\approx 1.6$. Such a finding implies, that the voltage response of the superconductor does not depend on temperature any more, suggesting that quantum creep [27] may take over at these low temperatures. This hypothesis is further supported by comparing the creep parameter $U_c/k_BT$ extracted from fitting the data for various temperatures, see Fig. 7(b). Their variations for temperatures above 3.5 K

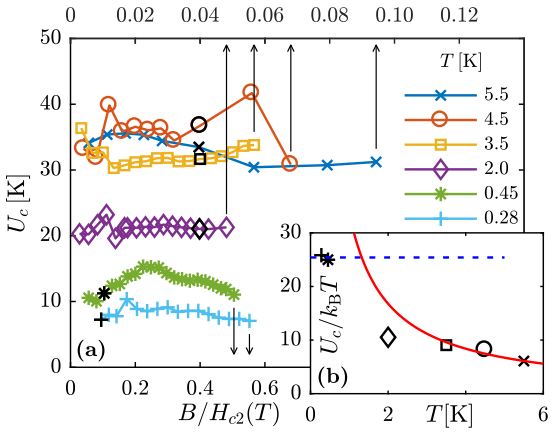


FIG. 7. (a) Activation barriers $U_c$ in $a$-MoGe versus magnetic field strength; lower and upper field axes refer to low ($T = 0.28$ K and 0.45 K) and high temperature data. The decrease of $U_c$ with decreasing temperature $T$ can be explained in terms of a crossover to quantum creep, see inset. (b) Plotting the dimensionless thermal creep parameter $U_c/T$ versus temperature (see black markers; we chose similar values of the reduced field), one observes a crossover to a constant value at low temperatures, that is consistent with a saturation of $U_c/T$ (solid red line for a constant $U_c \approx 34$ K) at the dimensionless action $S_c/\hbar$ quantifying quantum creep (dashed blue line for a constant action $S_c$) when the latter takes over at small temperatures.

are consistent with a value $U_c \approx 30 - 40$ K, see 7(a). Extrapolating the ratio $U_c/k_BT$ to the low-temperature region results in values larger then observed, and hence much lower vortex velocities. This suggests that the thermal creep parameter $U_c/k_BT$ saturates at its quantum analog $S/\hbar$, see Fig. 7(b); the latter produces a still appreciable (quantum) creep velocity $v \propto e^{-S/\hbar}$, with $S/\hbar < U_c/k_BT$. Alternatively, the sample may have dropped out of equilibrium with a measured temperature $T$ different from the actual 'temperature' of the sample, e.g., due to the presence of noise, see Ref. [2].

## IV. ACTIVATION BARRIERS

On a phenomenological level, creep-type vortex motion is a thermal process with vortices escaping from defects by overcoming a drive-dependent activation barrier $U(j)$; vortex motion then follows an Arrhenius-type formula for the velocity $v = v_{\rm th}e^{-U(j)/k_BT}$. In comparison, our equation (5) for the current–velocity characteristic describes creep-type motion as well, but follows from a quantitative determination [5 and 6] of the pinning force density $F_{\rm pin}(v,T)$ entering the force-balance equation (1). In the following, we show how these phenomenological and microscopic approaches relate to one another within strong pinning theory.

The interest in the activation barrier $U(j)$ is usually focused onto two limits: i) at weak drives $j \to 0$, barriers either remain finite or diverge, characterizing a vortex-liquid or a vortex-glass state, respectively [19], and ii) at drives $j \to j_c$, the barriers are expected to vanish, $U(j) \approx U_c(1-j/j_c)^\alpha$, with an exponent $\alpha$ depending on the pinning model. Strong pinning theory predicts [5 and 6] a saturating barrier and a thermally assisted flux-flow response at $j \to 0$. In the region near the critical drive $j_c$ relevant in this study, the barriers vanish with an exponent $\alpha = 3/2$; this result is universal for any smooth pinning potential. However, strong pinning theory provides us with the further insight that the appropriate variable in the barrier's scaling law is the pinning-force density $F_{\rm pin}(v,T)$ rather then the Lorentz-force density $F_{\rm L}$, see Eq. (3).

The standard result with the exponent $\alpha = 3/2$ is straightforwardly derived from our microscopic description in the limit where the viscous force $-\eta v$ in Eq. (1) (or the term $v/v_c$ in Eq. (5)) can be neglected. In this situation, the characteristic (5) is equivalent to the Arrhenius law with a barrier exponent $\alpha = 3/2$: indeed, within this approximation, the driving force $F_{\rm L}/F_c = j/j_c$ is balanced by the pinning force $F_{\rm pin}(v,T)/F_c = [(k_BT/U_c)\log(v_{\rm th}/v)]^{3/2}$ and our $v$–$j$ characteristic (5) can be cast into an Arrhenius-law with a barrier $U(j) = U_c(1-j/j_c)^{3/2}$.

Upon increasing the drive $j$, however, the vortex velocity $v$ becomes significant and the viscous term $-\eta v$ can no longer be neglected. Combining Eq. (3) and the equation of motion (1), we replace $F_{\rm pin} = F_{\rm L} - \eta v$ to obtain a barrier that depends on both drive $j$ and velocity $v$ in the form

$$U[F_{\rm pin}(v,T)] = U_c\Big(1 - \frac{F_{\rm L} - \eta v}{F_c}\Big)^{3/2} \qquad (7)$$

$$= U_c\Big[1 - \Big(\frac{j}{j_c} - \frac{v}{v_c}\Big)\Big]^{3/2} \equiv U(j,v). \qquad (8)$$

Using this expression for the barrier, the characteristic given by Eq. (5) can be written as a *self-consistent* Arrhenius law for the vortex velocity $v(j)$,

$$v = v_{\rm th}e^{-U(j,v)/k_BT}. \qquad (9)$$

Alternatively, using the data of the scaled $j$–$v$ characteristic, the expression (8) provides us with a direct access to the activation barrier $U(j,v)$. Indeed, plotting $-\log(v/v_c)$ versus $j/j_c - v/v_c$, we represent $U[F_{\rm pin}(v,T)]/k_{\rm B}T + \gamma$ versus $F_{\rm pin}(v,T)/F_c$ with the offset $\gamma = \log(v_c/v_{\rm th})$. Fig. 8 shows a typical outcome of arranging the data in this new manner. We then can follow two strategies, i) either assume the validity of (8) and use this fitting ansatz to extract the creep parameters $U_c/k_{\rm B}T$ and $v_{\rm th}/v_c$, or ii) interpret the data as directly providing the functional form of $U[F_{\rm pin}(v,T)]$, up to a constant. In doing so, we have to be careful to interpret the quantity $k_{\rm B}T\log(v_{\rm th}/v)$ as a barrier only if $v \ll v_{\rm th}$, corresponding to $U > k_{\rm B}T$; as $v \gtrsim v_{\rm th}$, the motion crosses over to vortex-flow and the interpretation in terms of a creep barrier breaks down.

The parameters $U_c$ and $v_{\rm th}/v_c$ shown in Figs. 4 (c) and (d) and in Fig. 7(a) have been obtained by following the procedure i). In extracting the parameter $U_c/k_{\rm B}T$, we have to select the appropriate portion of the curve: starting at $j/j_c - v/v_c = 1$ in Fig. 8(a) (corresponding to $F_{\rm pin}/F_c = 1$), the quantity $-\log(v/v_c)$ initially grows with a concave shape, goes through an inflection point, and then continues in a convex curve at smaller values $F_{\rm pin}/F_c < 0.9$. The initial concave form for $F_{\rm pin}$ close to $F_c$ originates from the saturation of $F_{\rm pin}(v,T) \to F_c$ when the velocity $v$ increases beyond the thermal velocity $v_{\rm th}$; this part of the curve is flow-dominated and is further discussed below. The creep-dominated region at small velocities corresponds to the convex region in Fig. 8 and it is this region that provides us with the value for the reduced barrier $U_c/k_{\rm B}T$. The ratio $v_{\rm th}/v_c$ derives from the condition $U[F_{\rm pin}(v,T)/F_c = 1] = 0$, i.e., the offset $-\gamma$ in $-\log(v/v_c)$ at $j/j_c - v/v_c = 1$, once the curve $U[F_{\rm pin}(v,T)]$ has been fitted and extrapolated to $F_{\rm pin}/F_c = 1$.

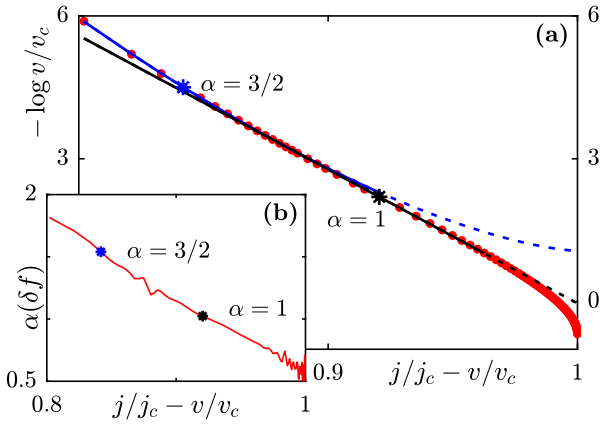


FIG. 8. Analysis of activation barriers for 2H-$NbSe_2$, with data for $B = 1.0\,$T, $T = 5.2\,$K represented by red dots. Shown are the $j$–$v$ data represented as $-\log(v/v_c) = U/k_{\rm B}T + \gamma$ versus $j/j_c - v/v_c = F_{\rm pin}/F_c$. The activation barrier $U(F_{\rm pin})$ in (a) is fitted to $U(F_{\rm pin}) = U_c(1 - F_{\rm pin}/F_c)^\alpha$ for different exponents $\alpha = 3/2$ (blue) and $\alpha = 1$ (black). The fits outside the range of validity $v < v_{\rm th}/e$ are continued with dashed curves. The inset (b) shows the construction of points $\alpha = 1$ and $\alpha = 3/2$ around which the fitting is done.

In a systematic fit, we search for the region that is best described by Eq. (8). We define the rescaled pinning force $\delta f = 1 - F_{\rm pin}/F_c$ and take the derivative $\partial_{\delta f}\log(v_c/v)$ in order to eliminate the constant shift $\gamma$; taking the log-derivative, we obtain $\alpha(\delta f) = 1 + \partial\log[\partial_{\delta f}\log(v_c/v)]/\partial\log(\delta f)$ as shown in the inset Fig. 8(b). The fit to Eq. (5) then is done around the point $\delta f^*$ for which $\alpha(\delta f^*) = 3/2$.

In following the alternative procedure ii) instead, we directly obtain the shape of $U(F_{\rm pin})$ (up to a constant shift) but miss its analytic form. In an attempt to extract some effective functional form, we can make some more progress by using our findings for the local exponent $\alpha(\delta f)$, see Fig. 8(b). For instance, it is possible to find a region at higher currents in Fig. 8(a) where the barrier shape is better characterized by an exponent $\alpha = 1$, reminding about Anderson's original scaling Ansatz for the creep barrier [4]. In Fig. 8(a), we compare separate fits to the data with $\alpha = 3/2$ (blue line) and $\alpha = 1$ (black line). At first sight, the fit for $\alpha = 1$ looks rather good, in particular at higher drives. Indeed, the changeover from a convex to a concave form at large pinning forces $F_{\rm pin}$ produces an inflection point in $-\log(v/v_c)$ with a region where the exponent $\alpha = 1$ quite naturally provides a better match to the data. However, this region close to $j_c$ is flow- rather than creep-dominated, with a barrier of order or even smaller than $k_{\rm B}T$. As discussed further below, the flow-dominated motion close to critical results in a concave shape of the function $-\log(v/v_c)$ versus $j/j_c - v/v_c$, that mimics a smaller exponent $\alpha = 1/2$ when translated to a 'barrier' $U \approx U_c(\delta f)^\alpha$. It then is the region at smaller drives and velocities where creep effects are expected to manifest in a clean and unperturbed manner. At these smaller drives, the exponent $\alpha = 3/2$ provides a consistent description of the experimental data. Going to even smaller drives, our expansion $U \propto (\delta f)^{3/2}$ is expected to break down [6] since higher-order corrections become relevant, $U \approx U_c[(\delta f)^{3/2} + c(\delta x)^{5/2} + \ldots$, that manifest in a larger local exponent $\alpha(\delta f) > 3/2$. Choosing a value $\alpha > 3/2$ indeed provides an inferior fit to the data.

In our discussion above, we have used the inset (b) in Fig. 8 as a tool to find the optimal location for our fits $U \propto (\delta f)^\alpha$ with different exponents $\alpha = 3/2$ and $\alpha = 1$ in the main figure (a). On the other hand, it is tempting to read the curve $\alpha(\delta f)$ as a physical result providing us with a critical exponent, in which case one expects a saturation $\alpha(\delta f \to 0) \approx 3/2$ that is not observed in our data. Rather, we observe a decrease in $\alpha$ below 3/2 at small $\delta f$ due to the mixing of creep-type- with flow-type motion when $U < T$ and an increase beyond 3/2 at large $\delta f$ due to corrections in the expansion of $U(\delta f)$.

A proper measurement of the critical exponent relies on the availability of a large range $\delta f \to 0$ within the critical region. In the present situation, this requires small temperatures $T$ in order to guarantee creep-type motion with $\alpha = 3/2$ deep into the critical region.

Finally, we comment on some subtleties in using the high velocity data for the extraction of $v_c$ (via $\rho_{\rm ff}$) and $j_c$. The strong pinning theory provides a detailed picture of vortex motion on several velocity scales: thermal creep [5 and 6] as discussed above affects the vortex response only at velocities below $v_{\rm th}$. Beyond $v_{\rm th}$, creep effects eventually become irrelevant and the finite temperature creep- and $T = 0$ excess-current characteristics merge. This merging in a shifted linear flux-flow characteristic manifests in the data as a saturation of the differential resistance, see Fig. 9(a).

In performing accurate fits, it is important to have experimental data that goes beyond the merger at $v_{\rm th}$ and reaches some saturation in the differential resistance, as this part of the data allows for inferring the correct critical current density $j_c$ and flux-flow resistivity $\rho_{\rm ff}$ through linear extrapolation. In an ideal situation, the linear excess-current characteristic above $v_{\rm th}$ allows for a straightforward extrapolation. In reality, the characteristic is never perfectly linear and the extrapolation has to be done around some chosen point $I_0, V_0$ of the characteristic. In order to find the correct point $I_0$ around which to construct the linear extrapolation, we combine the creep dynamics discussed here with the results of the flow-dynamics described in Refs. [14 and 15].

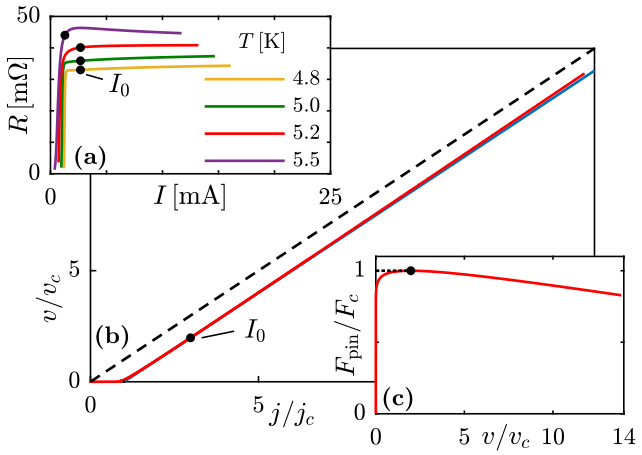


FIG. 9. Data for 2H-$NbSe_2$ ($B = 1.0\,$T) covering the complete measured range of currents. (a) The differential resistance $R = dV/dI$ exhibits a sharp increase and then becomes flat near the flux-flow resistance $R_{\rm ff}$; for the case of $T = 5.5\,$K, the resistance goes through a maximum at low drives, while we expect a broad maximum at larger drives for the other temperatures. The black dot marks the current $I_0$ chosen for the linear extrapolation. (b) Current–velocity characteristic (red for $T = 5.2\,$K) after rescaling the experimental data. The excess-current characteristic (blue straight line) is constructed by linear extrapolation around the current $I_0$. At large currents, the creep characteristic (red line) approaches the free flux-flow (dashed). (c) The pinning-force density $F_{\rm pin}$ (red for $T = 5.2\,$K) rises steeply towards the maximum value $F_c$ near the velocity $v_{\rm th}$ and then slowly decays, in agreement with the theoretical prediction [15].

The generic strong pinning situation is characterized by a separation of scales $v_c \ll v_p$, where $v_p \sim f_p/\eta a_0^3$ is the velocity scale for dissipative vortex motion within the defect potential excerting typical forces $f_p$. The excess current–voltage curve then is expected to turn back towards *free* flux-flow (see dashed blue line in Fig. 10(a)) only at velocities larger than $v_p$. Provided that $v_{\rm th} \ll v_p$, one thus expects the differential resistance to rise sharply towards $R_{\rm ff}$ on the scale $v_{\rm th}$, then going through a broad maximum within the extended velocity region $v_{\rm th} < v < v_p$, and returning from above to the free flux-flow branch and hence to $R_{\rm ff}$ at very large currents $v \gg v_p$, see the sketch (green line) in Fig. 10(b). This behavior is well in line with the behavior of the characteristics in Fig. 9 at the three lower temperatures. For the data measured at $T = 5.5\,$K (magenta line in Fig. 9(a)) the maximum is sharper and appears at lower drives. This is consistent with the scenario shown in Fig. 10(b), red line, where $v_p$ is of the order of $v_{\rm th}$. In this case, the differential resistance overshoots $R_{\rm ff}$ and goes through a more narrow maximum close to $v_{\rm th}$.

In choosing the point $I_0$ where the extrapolation to the excess-current characteristic (blue line in Fig. 9(b)) should be done, we should stay below the maximum in $R$ (i.e., below the inflection point of the current–voltage characteristic), ideally at the crossing of the differential resistance $R$ with the flux-flow resistance $R_{\rm ff}$. In particular, this educated choice guarantees that the extrapolation never crosses the $I$–$V$ characteristic but rather touches the latter in a tangent at $I_0$. Unfortunately, the flux-flow resistance $R_{\rm ff}$ may not be accurately known, which leaves some arbitraryness in the choice of $I_0$. For the lowest three temperatures in Fig. 9(a), we have chosen a value $I_0 = 2.7\,$mA near the onset of the flat maximum in $R$ and remark that the extracted parameters do not differ significantly for somewhat different choices of $I_0$. For the highest temperature $T = 5.5\,$K, we have chosen a value $I_0 = 1.3\,$mA before the maximum (which is expected at values $R > R_{\rm ff}$); again, the precise choice of $I_0$ does not change the extracted pinning parameters in a significant manner. Note that the experimental access to such a high-velocity regime is quite problematic in general due to heating effects that may even destroy the sample; this type of analysis then is restricted to materials with a small ratio $j_c/j_0$.

The above discussion also sheds some more light on the concave region of the barrier plot $U(F_{\rm pin})$ in Fig. 8 close to $F_c$. Translating the behavior of the current–voltage and resistance curves in Fig. 10 to the pinning-force density $F_{\rm pin}(v)$, one notes that the latter exhibits a broad maximum or plateau $F_{\rm pin}(v_{\rm th} < v < v_p) \approx F_c$ for the case $v_p \gg v_{\rm th}$, while a more narrow maximum

around $v_{\rm th}$ is expected when $v_p \sim v_{\rm th}$. Indeed, the maximum in $F_{\rm pin}$ corresponds to the point $\rho/\rho_{\rm ff} = 1$ in Fig. 10(b) and the derivative $\partial_j \rho$, small (large) for the case $v_p \gg v_{\rm th}$ ($v_p \sim v_{\rm th}$), determines the curvature of $F_{\rm pin}$. In Fig. 9(c), we show the pinning-force density (with a broad maximum) extracted from the data at $T = 5.2\,$K. We then can expand $F_{\rm pin}(v)$ around its maximum and approximate $\delta f \propto [(v_0 - v)/v_c]^2$. Inverting and expanding for small $\delta f \ll 1$ provides us with the scaling $\log(v_0/v_c) - \log(v/v_c) \propto \delta f^{1/2}$. The appearance of the concave region in $-\log(v/v_c)$ close to $F/F_c j/j_c - v/v_c = 1$ in 8 with an exponent $\alpha \approx 1/2$, see inset, is thus the direct consequence of the maximum in $F_{\rm pin}$ at $F_c$.

## V. PARAMETERS FROM STRONG PINNING THEORY

The interaction of vortex lines with sufficiently strong defects gives rise to bistable solutions for the vortex lattice displacement; the appearance of such bistabilities is the hallmark of the strong pinning regime. The weak- to strong pinning crossover is characterized by the Labusch parameter [23 and 28] $\kappa = \max[-e_p''(r)]/\bar{C}$, comparing the maximum (negative) curvature of the defect pinning potential $e_p(r)$ near its edge with the effective vortex lattice stiffness $\bar{C}$; pinning is strong provided that $\kappa > 1$. A second condition on the applicability of strong pinning

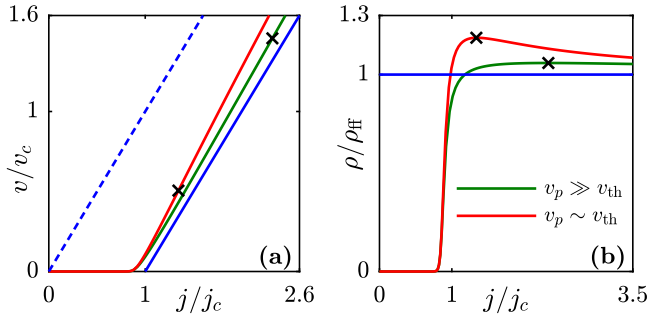


FIG. 10. Illustrative sketch of current–voltage characteristic (left, (a)) and differential resistance (right, (b)) for the two cases with $v_{\rm th} \ll v_p$ (in green) and $v_p \sim v_{\rm th}$ (in red); blue dashed (solid) lines are (shifted) flux-flow curves. The separation of scales is a necessary condition for the appearance of the straight excess-current characteristic in (a), see green curve. The scaled differential resistivity shown in (b) rises steeply on the thermal creep scale $v_{\rm th}$, overshoots the flux-flow resistance $R_{\rm ff}$, and then smoothly approaches $R_{\rm ff}$ from above. The resulting maximum (black cross) is broad when velocity scales are separated, $v_{\rm th} \ll v_p$ (in green); this reminds about the behavior seen in Fig. 9 for the lowest three temperatures. On the other hand, a more narrow maximum appears near $v_{\rm th}$ when $v_p \sim v_{\rm th}$ (in red), that resembles more the behavior of the high-temperature data at $T = 5.5\,$K in the experiment of Fig. 9.

theory is the independent action of individual pins, requiring that the density $n_p$ of pins is small, $n_p \xi^2 \kappa a_0 < 1$. Therefore, strong pinning does not necessarily imply a large critical current density $j_c$. As the density $n_p$ is increased above (or the field $B = \Phi_0/a_0^2$ decreased below) this condition, 3D strong pinning goes over into 1D strong pinning of individual vortices [29]. Below, we cite the main results of the 3D strong pinning regime as relevant in the present discussion and show how pertinent strong-pinning parameters such as $n_p$, $\kappa$, $f_p$, $U_c$ can be extracted from the comparison of theoretical predictions with experimental data, at least in principle.

Vortices (with a core of size $\xi$) remain pinned on a defect over an area $S_{\rm trap} \approx t_\parallel t_\perp$, with $t_\parallel \approx \kappa\xi$ and $t_\perp \approx \xi$ the longitudinal (along the vortex motion) and transverse trapping lengths. Assuming each defect to exert a pinning force $f_p \sim e_p/\xi$ ($e_p$ is the pinning potential depth) on the vortex, we find the maximal (or critical) pinning-force density $F_c = n_p(S_{\rm trap}/a_0^2) f_p$. When approaching the boundary of strong pinning at $\kappa \to 1$, the pinning-force density is reduced by a factor $(\kappa - 1)^2$ and we can make use of the interpolation formula

$$F_c \approx \gamma n_p (\xi^2 \kappa / a_0^2)(e_p/\xi)(1 - 1/\kappa)^2. \qquad (10)$$

The numerical $\gamma$ can be calculated once the specific shape of the pinning potential is known [5]; for the Lorentzian pinning potential $e_p(r) = e_p/[1 + (r^2/2\xi^2)]$, we find that $\gamma \approx 0.4$.

The intrinsic field- and temperature dependence of the critical current $j_c = cF_c/B$ follows from the corresponding dependencies of $e_p$, $\kappa$, and $\xi$. In the vicinity of the upper-critical field $H_{c2}(T) \approx H_{c2}(0)\,\tau$ with $\tau = 1 - T/T_c$, the coherence- and London penetration lengths scale as $\xi = \xi_0 \tau^{-1/2}$ and $\lambda = \lambda_0 \tau_b^{-1/2}$, respectively, with $\tau_b = \tau - b$ and $b = B/H_{c2}(0)$. Various pinning models involving metallic and insulating defects or $\delta T_c$-pinning, have been discussed in Ref. [30]; the pinning potential depth $e_p$ and the pinning strength $\kappa$ then depend in various ways on $\lambda$ and $\xi$. It turns out that the dominant contribution to the scaling near the $H_{c2}(T)$-line appears through the pinning energy $e_p = e_{p0}(1 - t - b)^{\beta_e}$ and the Labusch parameter $\kappa = \kappa_0(1 - t - b)^{\beta_\kappa}$ with model-dependent exponents $\beta_e$ and $\beta_\kappa$.

Scaling the critical current density $j_c = cF_c/B$ with the (zero-temperature) depairing current density $j_0 = (2/3\sqrt{3}) c H_c^2(0) \xi_0/\Phi_0$ (with $H_c(T)$ the thermodynamic critical field), we find that this ratio only involves the effective defect number in the trapping volume $n_p \xi^2 \kappa a_0 = n_p S_{\rm trap} a_0 < 1$ and the ratio $e_p/e_0 \lesssim 1$ with $e_0 = H_c^2(0)\xi_0^3/8\pi$ the (zero-temperature) condensation energy,

$$\frac{j_c}{j_0} \approx \frac{3\sqrt{3}\gamma}{16\pi}\, n_p \xi^2 \kappa a_0\, \frac{e_p}{e_0}\, \frac{\xi}{a_0}\, (1 - 1/\kappa)^2 (1 - T/T_c)^{1/2}. \qquad (11)$$

With $\kappa \propto a_0$, we find the typical strong-pinning scaling [15, 20, and 24] $j_c \propto 1/\sqrt{B}$. Upon decreasing the field below the 3D strong pinning condition $n_p S_{\rm trap} a_0 < 1$,

pinning turns one-dimensional (1D) and $j_c$ is expected to saturate to a $B$-independent value. Taking into account a weak $\kappa$-dependence of the transverse trapping $t_\perp \sim \kappa^{1/4}\xi$ [15] changes the field-scaling of the critical current density to $j_c \propto B^{-\alpha}$ with $\alpha = 5/8$ for a Lorentzian-shaped pinning potential. This result has been verified and augmented by numerical simulations [25] showing that the exponent $\alpha$ in fact decreases for increasing defect densities or vortex core size.

The result (11) tells, that $j_c$ should decrease on approaching the $H_{c2}(T)$-line, in agreement with the finding in Fig. 4(a). The scaling $j_c \propto B^{-\alpha}$ with exponents $\alpha \lesssim 0.5$ is observed in the data of Fig. 6 (a) and (b).

Next, we discuss the scale $U_c$ of the activation barrier. This turns out proportional to the pinning energy $e_p$, vanishes on approaching weak pinning $\kappa \to 1$, and only weakly depends on $\kappa$ for very strong pinning [5]; it is accurately described by the interpolation formula

$$U_c \approx \tilde{g} e_p \, (1 - 1/\kappa)^2 \tag{12}$$

with the numerical $\tilde{g} \approx 0.4$ for Lorentzian pinning potential. While the values of $U_c$ in Fig. 4(c) decrease rapidly on approaching the $H_{c2}(T)$-line, the data in Fig. 7 is more consistent with a constant value. Indeed, substantial variations of the barrier with field and temperature are to be observed only sufficiently close to the $H_{c2}(T)$-line; this is the case for 2H-$NbSe_2$ where $\tau_b < 0.16$. On the other hand, the data on $a$-MoGe has been obtained further away from the $H_{c2}$-line, with values of $\tau_b$ all larger than 0.2.

Comparing Eq. (11) for $j_c$ with the expression (12) for the activation barrier $U_c$ allows us to extract the effective defect number from the experimental data,

$$n_p \xi^2 \kappa a_0 \approx \frac{16\pi\tilde{g}}{3\sqrt{3}\gamma} \frac{j_c}{j_0} \frac{e_0}{U_c} \frac{a_0}{\xi} \frac{1}{(1 - T/T_c)^{1/2}}. \tag{13}$$

Given the values of $j_c$ and $U_c$, we can use Eq. (13) to find an estimate for the defect parameter $\kappa n_p a_0 \xi^2$; the data on 2H-$NbSe_2$ provides us with the values $\kappa n_p a_0 \xi^2 \approx (1.3, 1.7, 3.4, 12) \times 10^{-4} \ll 1$ at the four different temperatures, all consistent with the assumption of 3D strong pinning. With $\xi_0 \approx 77$ Å [31] and assuming a value of order unity for $\kappa$ provides the estimate $n_p \sim 2 \times 10^{15}\,\mathrm{cm}^{-3}$.

The density parameter $n_p \xi^2 \kappa a_0$ extracted from critical currents $j_c$ and activation barriers $U_c$ as derived from the fits on the $a$-MoGe films, see Figs. 6 and 7, is shown as a function of field in Fig. 11. At large fields $B > 4$ T, the separation between vortices $a_0$ is smaller than the film thickness $d$, the density parameter $\kappa n_p a_0 \xi^2 < 1$ is small, and we expect 3D strong pinning. On decreasing the field, two things happen: i) as the distance $a_0$ between vortices (that equals the extent of the distortion along pinned vortices) drops below $d$, vortices are cut and we enter the 2D strong pinning regime that is still well described by our strong pinning theory but with a modified effective elasticity $\bar{C} \propto B$ involving only shear. As a result, the Labusch parameter scales as $\kappa \propto a_0^2$ and the critical current density $j_c \propto 1/B$. ii) With increasing density parameter $n_p \xi^2 \kappa a_0$, vortices become individually pinned, either as 1D lines (at high fields with $a_0 < d$) or as 0D Pearl vortices (at low fields with $a_0 > d$). In this case, the critical current density $j_c$ is expected to flatten and become independent of field $B$. The critical current density $j_c$ in Fig. 6 seems to flatten at the lowest fields (see data at $T = 3.5$ K and $T = 4.5$ K) that may indicate a crossover to a field independent 1D or 0D regime. Furthermore, the field scaling $j_c \propto B^{-\alpha}$ with an observed $\alpha$ between 0 and unity covers the range of expected behavior, however, without clear attribution to a specific regime. An accurate association with a specific pinning region then seems difficult in the low-field/high-density region, given the competition between the dimensional crossover and the density $n_p$ crossover. Finally, we can use the data to extract an estimate for the defect density: with $\xi_0 \approx 52$ Å and $\kappa$ of order unity, the defect density $n_p$ itself assumes a value of order $n_p \sim 1 \times 10^{17}\,\mathrm{cm}^{-3}$.

Last, we turn our interest to the thermal velocity parameter $v_{\mathrm{th}}/v_c$. The theoretical prediction [5]

$$\frac{v_{\mathrm{th}}}{v_c} \approx \frac{T}{e_p} \frac{a(\kappa)}{n_p a_0 \xi^2} \tag{14}$$

is based on a simple particle-like ansatz in Kramer's rate expression [6, 21, and 22]; its proper evaluation, both theoretically and from experiment is notoriously difficult as it appears as the prefactor in the thermal activation rate which is dominated by the exponential factor with its activation barrier. Approximating $a(\kappa) \approx \tilde{a}\,(1 - 1/\kappa)^{-3/2}$ with a typical value $\tilde{a} \approx 0.1$, and using Eq. (12), we arrive at the simpler result

$$\frac{v_{\mathrm{th}}}{v_c} \approx \left[\frac{k_B T}{U_c} \frac{\tilde{a}\tilde{g}}{n_p \xi^2 \kappa a_0}\right] [\kappa\,(1 - 1/\kappa)^{1/2}], \tag{15}$$

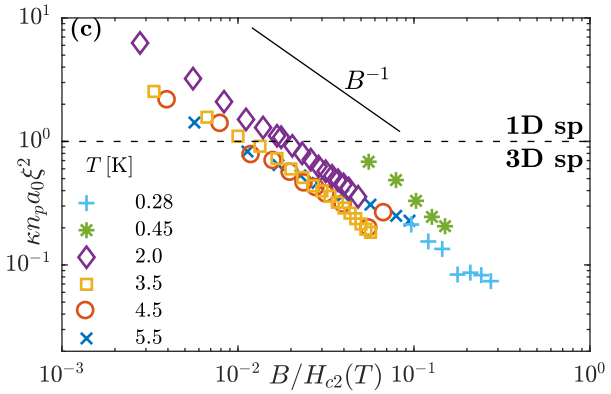


FIG. 11. Defect parameter $n_p \xi^2 \kappa a_0$ for $a$-MoGe as a function of magnetic field scaling with $\propto B^{-1}$, as expected from strong pinning theory. The dashed line marks the rough position of the expected crossover line between the 1D- and 3D-strong pinning regimes in the pinning diagram of Ref. [29].

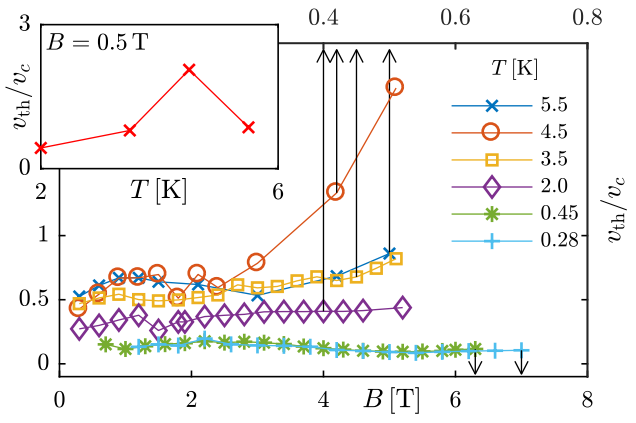


FIG. 12. Scaled thermal velocity $v_{\rm th}/v_c$ versus magnetic field $B$ for $a$-MoGe; upper and lower field axes refer to low ($T = 0.28\,\mathrm{K}$ and $0.45\,\mathrm{K}$) and high temperature data. The inset shows the dependence on temperature at a constant field $H = 0.5\,\mathrm{T}$, with a non-monotonic dependence as found before in the data for 2H-$NbSe_2$, see Fig. 4(d).

where we have suitably factorized the result for later convenience, see below. This result predicts an increase of $v_{\rm th}/v_c$ with temperature (due to the factor $k_{\rm B}T/U_c$) that is consistent with the findings obtained from fitting the characteristic, see Figs. 4(d) and 12, apart from the datapoint at the highest temperature. This might be explained by a collapse of the factor $(1-1/\kappa)^{1/2}$ near the $H_{c2}$-line that occurs in several of the pinning models discussed in Ref. [30].

Alternatively, the first factor of Eq. (15) can be evaluated using the experimental findings for $U_c$ and values for $n_p\xi^2\kappa a_0$ from Eq. (13) (derived from experimental results for both $U_c$ and $j_c$); such an analysis provides a result of order unity for the first factor, about an order of magnitude larger than the values extracted from the characteristic shown in Fig. 4(d). Consistency then would require $\kappa$ to be close to unity, i.e., individual pins are marginally strong. Repeating this analysis for $a$-MoGe and using known experimental results for $U_c$ and $j_c$, we find a small value of order $10^{-2}$ for the first factor in Eq. (15). One then concludes that the Labusch parameter $\kappa$ should be large in $a$-MoGe in order to reach consistency with the results in Fig. 12. However, a word of caution is in place here, as both our theoretical knowledge on the preexponential factor $v_{\rm th}/v_c$ as well as our precision to extract a reliable value from Fig. 8 are quite limited at this stage.

## VI. SUMMARY AND CONCLUSION

By applying the quantitative theory of strong pinning to current–voltage measurements, we provided a first quantitative data-driven analysis of vortex creep in the critical region and thus demonstrated the potential of the strong-pinning paradigm for explaining pinning and creep in superconductors. The strong pinning paradigm comes with a number of microscopic assumptions: defects have to be strong, i.e, they must generate bistable pinning states, and their density has to be small such that they act independently.

In return, we obtain specific phenomenological predictions: the critical current density follows a field-scaling $j_c \propto B^{-\alpha}$ with $\alpha \approx 0.5$ that is different from weak collective pinning theory and pinning persists well-beyond the critical drive that results in a linear excess-current characteristic. The experimental data analyzed in our work satisfies these requirements and provides a coherent picture when submitted to a strong pinning analysis. Studying 2H-$NbSe_2$ and $a$-MoGe with moderate critical temperature, we demonstrated that high temperature is not a necessary requirement for significant creep effects on the current–voltage characteristic. Indeed, the sensitivity of the characteristic to thermal fluctuations follows from the creep parameter $U_c/k_{\rm B}T$ which becomes small near the upper-critical field; temperature- and field variations of $U_c$ then have a large influence on the characteristic and are visible through thermal creep effects.

The barriers $U_c$ extracted from the fits can be compared with experiments on persistent current relaxation quantified by the normalized creep rate $S = -\partial \log j/\partial \log t$ [19]. Assuming that the activation barrier $U(j)$ vanishes with a characteristic exponent $\alpha = 3/2$, the creep rate is related to the barrier through $S \approx (2/3)(k_{\rm B}T/U_c)^{2/3}$ [6]. Fitting the data of 2H-$NbSe_2$ for $T = 4.8\,\mathrm{K}$ yields the barrier $U_c \approx 980\,\mathrm{K}$, see Fig. 4, a value that is consistent with the observed creep rate [32] ranging from $S \approx 5\times10^{-3}$ to $S \approx 10^{-2}$.

It is also important to stress that while the prefactor $U_c$ defines the barrier scale due to the defect potential (and is comparable to the defect pinning energy $e_p$), the actual barrier $U(F_{\rm pin})$ relevant for creep is much reduced due to the drive, what renders the creep motion visible in the experiment. For large drives, this barrier eventually drops below the fluctuation energy $k_{\rm B}T$ and Kramer's rate theory breaks down. This restricts the applicability of our results and thus the reliability of the fits to the region $v < v_{\rm th}/e$. At large velocities $v > v_p$ with $v_p \gg v_{\rm th}$, dynamical effects become important and experimental data covering such a region far beyond the critical current then show a collapse of the pinning force and an approach towards the free flux-flow, again in agreement with the strong pinning theory.

Following the prediction of strong pinning theory that the activation barrier $U(F_{\rm pin})$ depends on the pinning-force density $F_{\rm pin}$ rather than the driving current density $j$, we have proposed a new methodology to extract the creep parameters $U_c/k_{\rm B}T$ and $v_{\rm th}/v_c$, the barrier and prefactor in the Arrhenius law for the activated process. In comparison to the standard assumption of a barrier dependence $U(j/j_c)$, the strong pinning expression includes the dissipative force as well, $U(j/j_c - v/v_c)$; the two Ansätze coincide in the region of very small veloc-

ities or large barriers, where the dissipative term can be ignored, $v/v_c \ll j/j_c$. Analyzing our data, it turns out that this correction is relevant: e.g., for $a$-MoGe and $T = 3.5\,\mathrm{K}$ (Fig. 5), we find that $v/v_c \approx 0.11$ for $j = 0.8 j_c$; hence, neglecting the viscous term would lead to a shift $\delta j \approx 0.11 j_c$ of the theoretical prediction and hence a significant deviation from the experimental data. Finally, the intriguing saturation of the creep parameter $U_c/k_{\mathrm{B}}T$ in $a$-MoGe at low temperatures points to the possibility of performing a direct observation of quantum creep through current–voltage measurements, that could be verified by future experimental and theoretical work.

## ACKNOWLEDGMENTS

We thank Kristin Willa, Eli Zeldov, Marcin Konczykowski, and Roland Willa for inspiring discussions. M.B. acknowledges financial support of the Swiss National Science Foundation, Division II. Z.L.X. acknowledges supports by the U.S. Department of Energy, Office of Science, Basic Energy Sciences, Materials Sciences and Engineering and the National Science Foundation under Grant No. DMR-1901843.

[1] A. A. Abrikosov, [Zh. Eksp. Teor. Fiz. **32**, 1442 (1957)] JETP **5**, 1174 (1957).
[2] S. Dutta, I. Roy, S. Mandal, J. Jesudasan, V. Bagwe, and P. Raychaudhuri, "Extreme sensitivity of the vortex state in a-moge films to radio-frequency electromagnetic perturbation," (2019), arXiv:1909.06573 [cond-mat.supr-con].
[3] J. Bardeen and M. J. Stephen, Physical Review **140**, A1197 (1965).
[4] P. W. Anderson, Phys. Rev. Lett. **9**, 309 (1962).
[5] M. Buchacek, R. Willa, V. B. Geshkenbein, and G. Blatter, Phys. Rev. B **98**, 094510 (2018).
[6] M. Buchacek, R. Willa, V. B. Geshkenbein, and G. Blatter, Phys. Rev. B **100**, 014501 (2019).
[7] Z. L. Xiao, E. Y. Andrei, Y. Paltiel, E. Zeldov, P. Shuk, and M. Greenblatt, Phys. Rev. B **65**, 094511 (2002).
[8] I. Roy, S. Dutta, A. N. Roy Choudhury, S. Basistha, I. Maccari, S. Mandal, J. Jesudasan, V. Bagwe, C. Castellani, L. Benfatto, and P. Raychaudhuri, Phys. Rev. Lett. **122**, 047001 (2019).
[9] P. W. Anderson and Y. Kim, Rev. Mod. Phys. **36**, 39 (1964).
[10] Y. B. Kim, C. F. Hempstead, and A. R. Strnad, Phys. Rev. **131**, 2486 (1963).
[11] C. P. Bean, Phys. Rev. Lett. **8**, 250 (1962).
[12] Y. Yeshurun, A. Malozemoff, and A. Shaulov, Rev. Mod. Phys. **68**, 911 (1996).
[13] H. Safar, P. L. Gammel, D. J. Bishop, D. B. Mitzi, and A. Kapitulnik, Phys. Rev. Lett. **68**, 2672 (1992).
[14] A. U. Thomann, V. B. Geshkenbein, and G. Blatter, Phys. Rev. Lett. **108**, 217001 (2012).
[15] A. U. Thomann, V. B. Geshkenbein, and G. Blatter, Phys. Rev. B **96**, 144516 (2017).
[16] B. Sacépé, J. Seidemann, F. Gay, K. Davenport, A. Rogachev, M. Ovadia, K. Michaeli, and M. V. Feigel'man, Nature Physics **15**, 48 (2019).
[17] A. R. Strnad, C. F. Hempstead, and Y. B. Kim, Phys. Rev. Lett. **13**, 794 (1964).
[18] A. I. Larkin and Y. N. Ovchinnikov, Journal of Low Temperature Physics **34**, 409 (1979).
[19] G. Blatter, M. V. Feigel'man, V. B. Geshkenbein, A. I. Larkin, and V. M. Vinokur, Rev. Mod. Phys. **66**, 1125 (1994).
[20] Y. N. Ovchinnikov and B. I. Ivlev, Phys. Rev. B **43**, 8024 (1991).
[21] H. Kramers, Physica **7**, 284 (1940).
[22] P. Hänggi, P. Talkner, and M. Borkovec, Rev. Mod. Phys. **62**, 251 (1990).
[23] G. Blatter and V. B. Geshkenbein, "Vortex matter," in *Superconductivity: Conventional and Unconventional Superconductors*, edited by K. H. Bennemann and J. B. Ketterson (Springer Berlin Heidelberg, Berlin, Heidelberg, 2008) pp. 495–637.
[24] W.-K. Kwok, U. Welp, A. Glatz, A. E. Koshelev, K. J. Kihlstrom, and G. W. Crabtree, Reports on Progress in Physics **79**, 116501 (2016).
[25] R. Willa, A. E. Koshelev, I. A. Sadovskyy, and A. Glatz, Superconductor Science and Technology **31**, 014001 (2017).
[26] A. I. Larkin and Y. N. Ovchinnikov, in *Nonlinear superconductivity* (Elsevier Science (Langenberger, D. N. and Larkin, A. I., editors), 1986) p. 493.
[27] G. Blatter, V. B. Geshkenbein, and V. M. Vinokur, Phys. Rev. Lett. **66**, 3297 (1991).
[28] R. Labusch, Crystal Lattice Defects **1**, 1 (1969).
[29] G. Blatter, V. B. Geshkenbein, and J. A. G. Koopmann, Phys. Rev. Lett. **92**, 067009 (2004).
[30] R. Willa, V. B. Geshkenbein, and G. Blatter, Phys. Rev. B **93**, 064515 (2016).
[31] S. Banerjee, N. Patil, K. Ghosh, S. Saha, G. Menon, S. Ramakrishnan, A. Grover, P. Mishra, T. Rao, G. Ravikumar, V. Sahni, C. Tomy, G. Balakrishnan, D. Paul, and S. Bhattacharya, Physica B: Condensed Matter **237-238**, 315 (1997), proceedings of the Yamada Conference XLV, the International Conference on the Physics of Transition Metals.
[32] S. Eley, K. Khilstrom, R. Fotovat, Z. L. Xiao, A. Chen, D. Chen, M. Leroux, U. Welp, and W.-K. Kwok, Scientific Reports **8** (2018), 10.1038/s41598-018-31203-0.